ADVANCED PHOTONICS RESEARCH
Open Access
www.adpr-journal.com

hBN-Encapsulated Graphene Coupled to a Plasmonic Metasurface via 1D Electrodes for Photodetection Applications

Christian Frydendahl, Sita Rama Krishna Chaitanya Indukuri, Taget Raghavendran Devidas, Zhengli Han, Noa Mazurski, Kenji Watanabe, Takashi Taniguchi, Hadar Steinberg, and Uriel Levy**

It is shown here how encapsulated graphene devices can be laterally coupled to plasmonic metasurfaces via 1D edge contacts, preserving the high mobility of encapsulated graphene while enhancing optical coupling. The device is used for photodetection applications where high responsivities in the range of 100 A W^{-1} for most of the visible spectrum are reported. The device exhibits a photogating effect which is attributed to defect states in the encapsulating hBN layers. The results highlight a new configuration to couple graphene with plasmonic structures and points to a new type of device based on defect states and graphene's excellent transport properties to achieve photodetectors with ultrahigh responsivities.

1. Introduction

The past two decades have seen a rush of new optical devices based on 2D material's unique optical properties.[1–3] There are numerous examples in the literature, from photoconductors,[4–7] bolometers,[8–12] photothermovoltaic devices,[13,14] optical field-effect transistors,[15–17] and heterostructure devices.[18,19] Photodetectors based on graphene are of particular note, as these devices offer optical detection across the entire electromagnetic spectrum,[1] a result of graphene's gapless dispersion relation and unique uniform optical absorption of ≈2.3% for most wavelengths.[20] This absorption is however still fairly low for photodetection purposes, and much of the recent literature has therefore focused on exploring graphene's integration with different photonic structures[1,3] or methods to pattern graphene itself into plasmonic nanopatterns to increase optical absorption.[21,22]

Graphene–photonic structure integration is usually done by placing metallic or dielectric nanostructures directly on top of or below the grapheme.[1,3,5,23–26] However, an important result in graphene device physics has been the fact that it is necessary to encapsulate graphene monolayers between two sheets of the insulating 2D material hexagonal boron nitride (hBN) to achieve ideal carrier transport characteristics.[27,28] This encapsulation ensures devices are chemically stable in ambient conditions, as graphene is protected from atmospheric adsorbates. Encapsulation also ensures atomically flat graphene sheets, enabling room-temperature ballistic transport.[27] As a result, encapsulation of graphene in hBN has rapidly become the standard platform in the device community and is likely to become the dominant platform in a potential future graphene device industry. Additionally, the growing field of twisted bilayer graphene is completely dependent on hBN encapsulation to manufacture the twisted bilayers. The strong van der Waals attraction between graphene and hBN is what enables the precise angular stacking of one part of a graphene crystal onto itself.[28,29]

Furthermore, encapsulation enables the fabrication of 1D "edge contacts" where the graphene sheet is connected to metal electrodes by a single row of carbon atoms.[27,30,31] Such contacts have shown superior performance in terms of contact resistance, generally attributed to the fact that the edge atoms of the graphene sheet are less strongly bonded (due to a lack of neighboring carbon atoms) and thus can more readily accept electrons from outside.[30,31] Contact resistance is an important parameter to optimize to ensure fast time-response electronics, due to the fundamental limits imposed by the effective device circuit's RC time constant on rise and fall times.

However, hBN encapsulation greatly limits how a graphene sheet can be coupled to plasmonic metasurfaces and nanoantennas. For example, plasmonic particles need to be positioned close to direct physical contact with the graphene sheet to enhance

C. Frydendahl, S. R. K. C. Indukuri, Z. Han, N. Mazurski, U. Levy
Department of Applied Physics
The Hebrew University of Jerusalem
Jerusalem 91904, Israel
E-mail: christia.frydendahl1@mail.huji.ac.il; ulevy@mail.huji.ac.il

T. R. Devidas, H. Steinberg
The Racah Institute of Physics
The Hebrew University of Jerusalem
Jerusalem 91904, Israel

K. Watanabe, T. Taniguchi
Advanced Materials Laboratory
National Institute for Materials Science
Tsukuba 305-0044, Japan

The ORCID identification number(s) for the author(s) of this article can be found under https://doi.org/10.1002/adpr.202300192.

DOI: 10.1002/adpr.202300192

optical absorption due to the short spatial extent of their optical near fields, and if injection of hot carriers from plasmonic decay is desired, then a direct electrical contact between the two materials is needed.[23,32] As a result, to our knowledge there have not yet been any studies so far into hot electron injection from plasmonic decay[33] into encapsulated graphene.

We report here a new type of graphene photodetector, with high responsivity in the visible regime based on charge injection from plasmon decay in a gold metasurface to an encapsulated sheet of graphene. The metasurface is contacted to graphene via 1D edge contacts and consists of a pattern of nanodisks/cones. The device configuration in the present work, a graphene layer doubly encapsulated by hBN, provides us with a 2D electron gas (2DEG) that has high carrier mobility and low intrinsic doping.

In addition to the hot carrier injection mechanism, we also observe a photogating effect in our device. While it is not fully clear from our immediate experiments what is the exact mechanism causing this, we speculate that it may be related to charge transfer from defect states that have been generated in the hBN where it was etched to form the metasurface. These defects act as artificial atoms and have discrete energy levels.[34,35] While of great interest in their own right, in particular as single-photon emitters for quantum light applications, here we speculate that their ability to have intrinsic charge is what is causing a photogating effect in our device. Upon being illuminated, the defect states release their trapped charges and change their charge polarity, resulting in a different external field affecting the graphene when the device is illuminated.[36,37]

We report large peak responsivities in the range of $\approx 100\,\mathrm{A\,W^{-1}}$ and a noise equivalent power (NEP) of $\approx 100\,\mathrm{pW}/\sqrt{\mathrm{Hz}}$ across the visible spectrum. It is important to mention that the device saturates for even nominal power increases and thus the responsivity may be even higher for lower optical powers than the ones tested here, further improving the NEP of the device. Our results highlight a new device design where graphene can be encapsulated in hBN, yet still be connected to plasmonic nanostructures to retain ideal transport properties. Additionally, the presence of the photogating effect points to a new intriguing class of devices where encapsulated graphene is coupled to deterministically generated defects in its encapsulating hBN.

2. Results

Figure 1a shows a schematic of the device and details the measurement configuration. The device is a regular encapsulated graphene field-effect transistor configuration with 1D edge-contacted source–drain electrodes and a backgate to the silicon substrate. In the same etching and metal evaporation step that defines the source–drain electrodes, a square lattice of nanodisks has been patterned. The result after metal evaporation is metal disks that penetrate into the hBN layers and attach to the graphene sheet at its edge atom sites. Optical microscope images of a finished device can be seen in Figure 1b,c, which shows scanning electron microscopy (SEM) images of another device, and

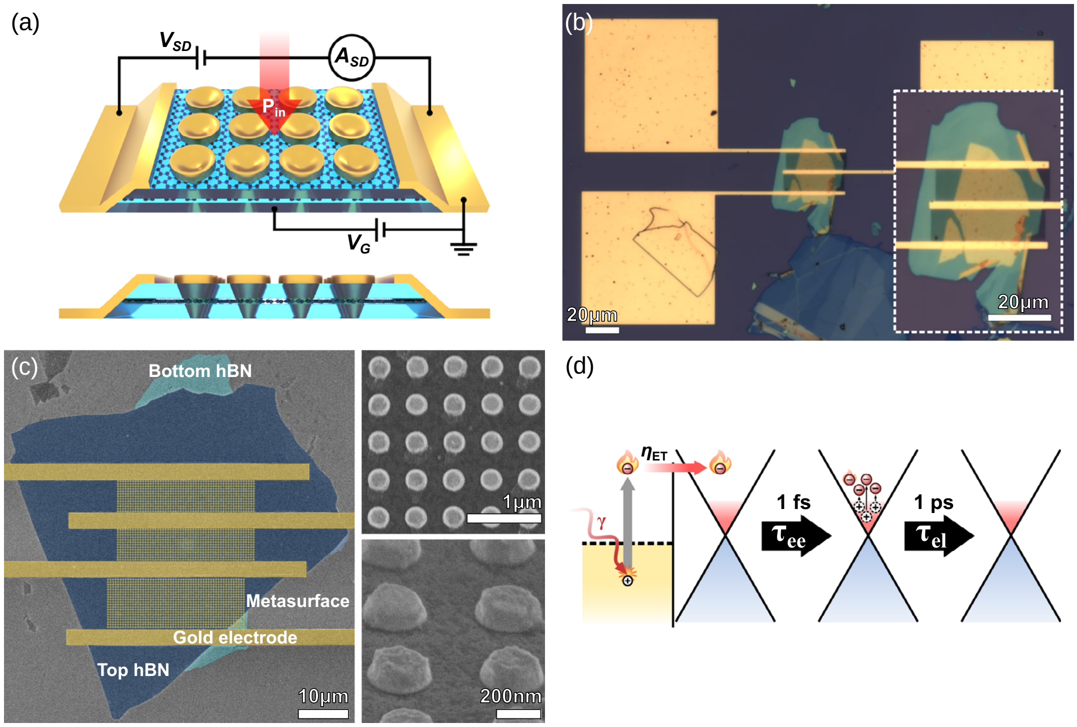

Figure 1. Device and working principle. a) Schematic of the device, with illumination scheme and electrical contact scheme detailed. b) Optical microscope image of a device. Scale bars are 20 μm. c) SEM image of a device, showing the metasurface dimensions. d) Hot carriers are generated in the gold upon optical absorption, which are then transferred to the graphene. Here they exchange energy with other electrons near the Fermi level, creating a continuum of hot electrons, before everything relaxes back to the lattice temperature.

Figure S1 and S2, Supporting Information, show atomic force microscope images of the 2D material layer profiles.

As the plasmonic structures are electrically connected to the graphene by 1D edge contacts, hot carriers generated in the gold can be transferred to graphene, where these carriers will induce a detectable change in graphene's conductivity, as shown in Figure 1d. The carrier mobility in graphene is inversely proportional to the carrier's energy, $\mu \propto 1/E$, while the electron–electron scattering time, τ_{ee}, is in the range of a few femtoseconds. This means a transferred hot carrier can quickly distribute its energy to multiple carriers near the Fermi level to create a continuum of hot carriers with a lifetime corresponding to the electron–lattice scattering time, τ_{el}, which in graphene is a few picoseconds. Thus the expected effect of hot carrier injection is an overall reduction in device conductivity.[11,12] Additionally, the transfer of additional electrons to graphene should cause a slight n-doping of the device.[32]

To understand where hot carriers could be generated in the samples, we have performed numerical finite-difference time-domain (FDTD) simulations of the nanodisk array together with the hBN and graphene stacks. For the geometry, disk diameters of 400 nm and a period of 500 nm were chosen, corresponding to the dimensions of the fabricated device (see Figure S2, Supporting Information). In accordance with the sloped shape of etched hBN layers (a result of the anisotropy of the reactive ion etching [RIE] process),[27] we have patterned the gold structures into a flattened inverted pyramid shape. The resulting electric field map for an incident wavelength of 750 nm can be seen **Figure 2**a, with the corresponding reflection and absorption spectra shown in Figure 2b. Absorption was calculated as $A = \frac{1}{2}\text{Im}[\varepsilon(x,y,z)]|E(x,y,z)|^2$, where $\varepsilon(x,y,z)$ and $E(x,y,z)$ refer to the dielectric function and the electric field in the full 3D space of the simulation. Thus, absorption is calculated as a function of how much the electric field intensity overlaps with lossy materials, such as gold. The reflection was recorded using a field monitor above the simulation region. From these simulations we see that the vast majority of the absorption occurs near the surface of the gold nanodisks, not in graphene sheets. This is consistent with plasmonically enhanced absorption in gold nanodisks.

Next, we perform a series of gate sweep measurements on the device, while illuminating it with various optical powers from a 600 nm laser source. While sweeping the gate voltage, V_G, we maintain a fixed source–drain voltage, $V_{SD} = 200$ mV, and measure the resulting source–drain current, I_{SD}. Some examples of the raw measurement data can be seen in **Figure 3**a. If we focus on the dark measurement first (the blue line in Figure 3a), then we see the characteristic field-effect-induced change of the graphene sheet's conductivity with the change in applied gate voltage. This is due to the back-gate-induced charge capacity affecting graphene's doping,[17,36] with the characteristic low point of current/conductivity corresponding to charge neutrality found at the applied gate voltage, $V_G = V_D$. Our initial device is slightly n-doped ($V_D < 0$). We see that for higher optical powers, the position of the charge neutrality point shifts to larger positive values of V_G, implying p-doping of the device with light (as larger amounts of induced n-doping are required to reach charge neutrality).

In terms of optical response of the device, this photodoping effect serves to enhance device responsivity by horizontally shifting the I_{SD}–V_G curves. We have included a schematic explanation of the effects observed in Figure 3b. Injection of hot carriers induces a decrease in device mobility, which results in a widening of the V-shape of the I_{SD}–V_G curve (as the mobility is proportional to the slope of this curve).[38] While we expected a shift to the left of the charge neutrality point, we observed a shift to right in our devices. This is indicative a p-doping photogating effect.

In Figure 3c, we have schematically illustrated how defect states created by the RIE process used to etch through the hBN encapsulation layers could be responsible. Dry etching/ion bombardment is a well-known method to create optically active defect states in hBN.[34,39,40] We observe wide-band fluorescence emission in the visible regime coming from the etched areas of our devices when illuminating them with an intense 532 nm laser, which is a common indication of hBN defects being present.[34,39,40] Such defects can be intrinsically charged and upon illumination could reverse their polarity due to detrapping. Thus, we suspect them to be the main candidate responsible for the observed photogating effect. A similar effect has been observed before with quantum dots deposited directly on top of a graphene layer.[37] If we track the shift of the neutrality point versus illumination power, we can also see that this effect saturates very rapidly for even nominal incident optical powers, as shown in Figure 3d. This is in agreement with previous observations.[32,37] When measuring the rise- and fall times of a device,

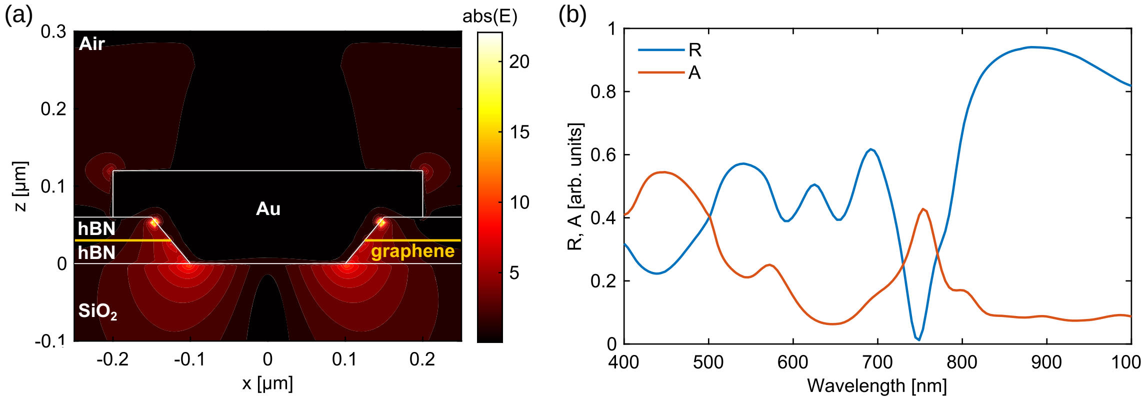

Figure 2. Optical design. a) Field intensity map around 750 nm wavelength and b) Simulated reflection and absorption spectra.

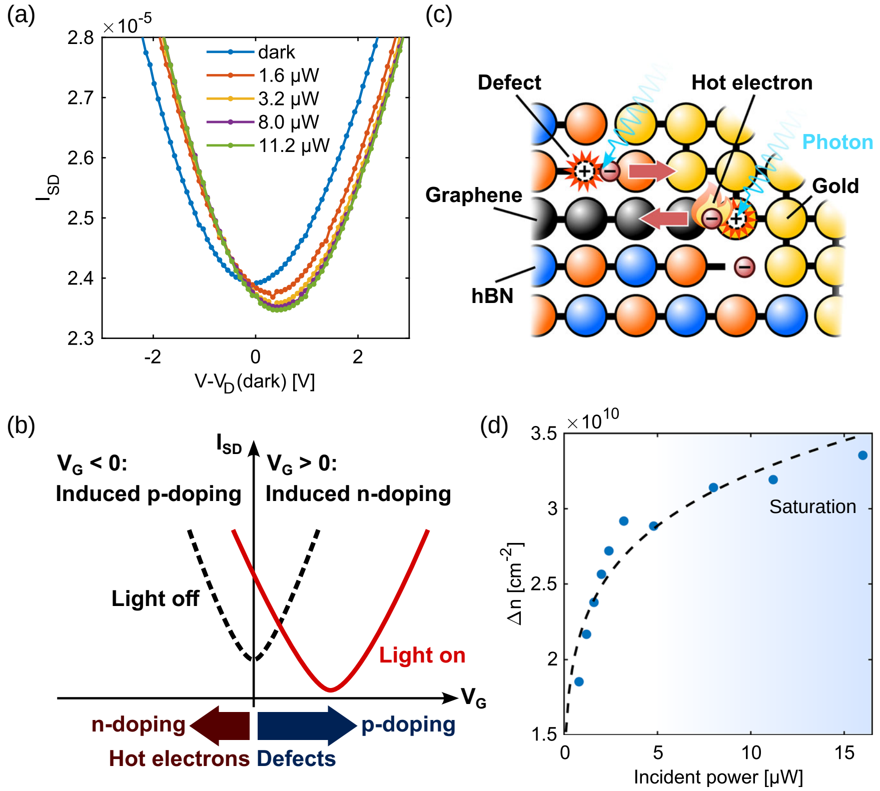

Figure 3. Optical response of the device. a) I_{SD} versus different gate voltages under different 600 nm laser illumination powers. The sample gets progressively more p-doped with increasing illumination powers. b) Schematic of the optical response. We expect to see n-doping from hot carrier transfer from plasmonic decay, but the total response is dominated by p-doping. We also see the general reduction in conductivity and device mobility associated with hot carrier injection/generation (deeper and wider V-shape in the I_{SD} curve). c) Schematic of physical mechanisms in the device. Defect states created during the RIE etching of the hBN could be responsible for the observed p-doping. d) Change in intrinsic charge carrier density, Δn, versus incident optical power. We see that the effect rapidly saturates for increasing power. Dotted line marks a power law fit.

we find them to be respectively ≈0.5 and ≈1 s (Figure S3, Supporting Information). Such slow time response is consistent with the long lifetimes associated with some hBN defect states of a few ms.[41]

We can calculate the device's optical responsivity as

$$R = \frac{I_{\text{light}} - I_{\text{dark}}}{P_{\text{dev}}} \tag{1}$$

with I_{light} as the device current under illumination, I_{dark} the dark current, and P_{dev} is the fraction of the total incident optical power, P_{in}, that hits the device, that is, $P_{\text{dev}} = P_{\text{in}}A_{\text{dev}}/A_{\text{spot}}$, with A_{dev} and A_{spot} respectively being the area of the active device region and the illumination laser spot area. If we plot the responsivity as a function of the device gate voltage, V_G, and the incident power, we get **Figure 4**a. In terms of optical intensities, we have illuminated the device area with roughly 41–162.5 mW cm^{-2} in Figure 4a. If we perform line cuts for a constant gate voltage, such as in Figure 4b, we see that the responsivity rapidly saturates for even nominal optical powers, both for the positive and for negative device response regimes. This is consistent with the photogating effect being the cause of large responsivity. From Figure 4c, we see that positive and negative regimes fall on either side of the charge neutrality point of the device, and the responsivity is exactly 0 for $V_G – V_D = 0$. We call our two different regimes of photoresponse bolometric and photoconductive (respectively for negative and positive values of R), although this is more or less just a choice to match convention for the sign of the responsivity. The true photoresponse mechanism of our device is likely that of a photogated bolometer.

If we track the magnitude of the charge neutrality point shift, Δn, versus the wavelength of the incident laser, we get **Figure 5**a. By measuring a reflection spectrum from the device metasurface area, and assuming the device has 0 transmission (due to silicon substrate), the absorption can be found approximately as 1 – Reflection. Then, we can map the device absorption spectrum, presented in Figure 5b. There appears to be a general correlation, such that increased optical absorption relates to an increase in charge neutrality point shift.

Finally, we characterize the noise spectral density (NSD) of our device's dark current (see Experimental Section for details), as shown in Figure 5c. From the NSD, we can calculate the NEP as NSD at 1 Hz bandwidth divided by responsivity, and we get Figure 5d. We see that our device has NEP of ≈100 pW/$\sqrt{\text{Hz}}$, for the lowest incident powers. In Figure 5e, we show the mobility of a typical device versus induced doping from the gate potential. We see that our device maintains peak mobilities in the range of 7000 cm^2 V^{-1} s^{-1}.

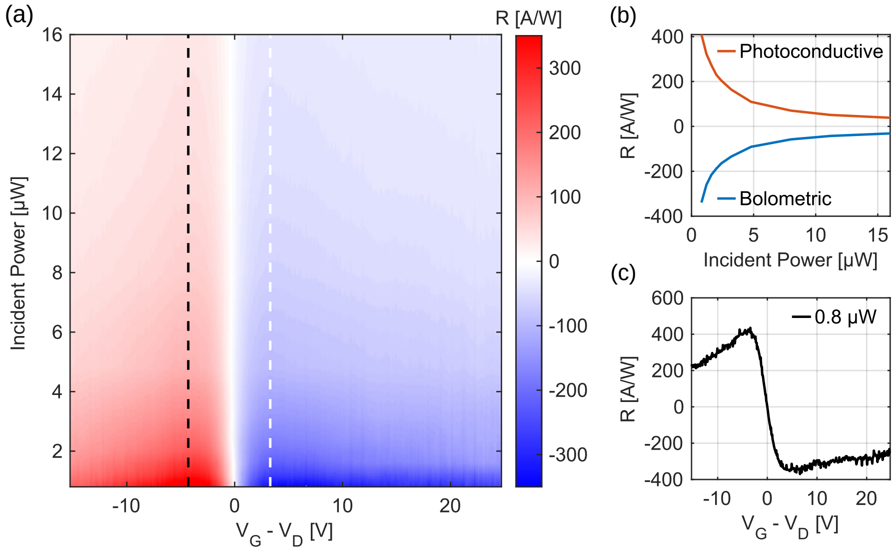

Figure 4. Responsivity versus incident power. a) Responsivity contour plot for different incident powers with 600 nm and gate potentials. b) Line cuts from (a) black dotted line corresponds to the photoconductive regime (positive *R*) and the white dotted line corresponds to the bolometric regime (negative *R*). We see that the responsivity rapidly saturates for increasing powers. c) Responsivity versus gate voltage for a fixed incident power.

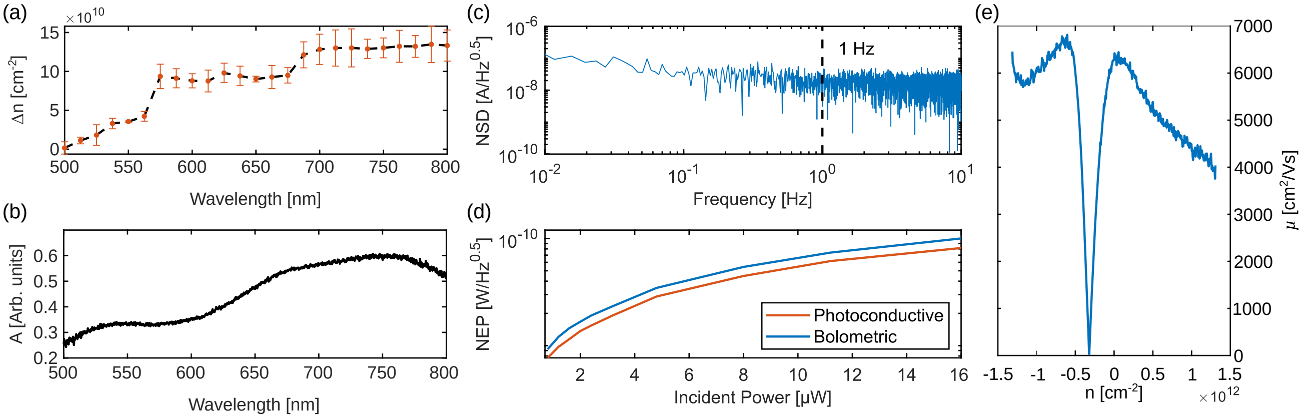

Figure 5. Dirac point shift versus wavelength and noise. a) Shift in Dirac point versus laser wavelength. All points are recorded with 16 μW power. Error bars correspond to uncertainty on fitting parameters. b) Optical absorption spectra recorded from the device. c) NSD of a device at $V_G = 0$ V. d) NEP for the responsivity curves shown in Figure 3b. e) Mobility versus induced doping in a device at room temperature without illumination.

3. Discussion

A surprising result is the observed p-doping of graphene when the device is exposed to light. While the exact cause is outside the scope of this investigation, one potential explanation is the generation of defect states in hBN, when it is exposed to high-energy electrons during electron beam lithography (≈100 keV) and then subsequently etched in the RIE step to make 1D electrical contacts. hBN hosts a very large variety of potential defect states, many of which hold intrinsic charge, either positive or negative.[42] The most common types are boron or nitrogen vacancies, either with or without carbon substitutions.[43] As our RIE process directly exposes hBN to carbon in the form of a CHF_3 plasma, such carbon substitution defects could likely occur in our specific case.

When the device is illuminated, the charges trapped in the defect states can be released and transferred to graphene, where they get carried away by the bias voltage. Left behind however are the oppositely charged defects in hBN, which contribute a small opposite electrostatic field upon graphene, changing its doping.[44] Another potential explanation is intrinsic defect states in hBN (from lower-quality hBN crystals) or contaminants trapped in the hBN/graphene interface during heterostructure assembly. High-spatial-resolution photocurrent maps could help to clarify this in a future study.

A similar photogating of graphene has been reported before, using charge transfer from quantum dots attached to graphene,[37] and it seems likely that defects in hBN could serve a similar function in our device. When recording Raman spectra to verify the chemical integrity of the graphene after the fabrication process (see Figure S4, Supporting Information), we did notice a significant amount of hBN defect fluorescence (broad visible spectrum emission). As the graphene sheet is exposed over most of its area to etched hBN (along every edge of the gold nanodisks), the effect of such defect doping would be greatly amplified, even for nominal defect densities in the etched areas.

If we calculate the thermal/Johnson current noise as

$$I_{n,\mathrm{thermal}} = \sqrt{\frac{4k_\mathrm{B}T\Delta f}{R_\mathrm{s}}} \tag{2}$$

where k_B is Boltzmann's constant, T is temperature, Δf the bandwidth, and R_s is the serial resistance of our device ($\approx 8\ \mathrm{k\Omega}$), we get $I_{n,\mathrm{thermal}} \approx 1.44\ \mathrm{pA}/\sqrt{\mathrm{Hz}}$ at a bandwidth of 1 Hz. We see our device is dominated by a general white noise background. As the measured NSD at 1 Hz is $\approx 20\ \mathrm{nA}/\sqrt{\mathrm{Hz}}$ (Figure 5c), which is significantly higher than the thermal noise, a possibility is that the current through the device experiences constrictions/tunnel barriers at points around the etched areas where the nanostructures are patterned (or even at the main source and drain electrodes), resulting in significant shot noise, similar to a Zener diode noise generator.

In terms of wavelength dependence, we see that the peak responsivity of the device follows the spectral shape of Figure 5a,b when illuminating with a fixed power for different wavelengths, see Figure S5, Supporting Information, for more details. This is consistent with the idea of plasmonically enhanced absorption and charge transfer from the gold metasurface, amplifying the graphene's intrinsic photoresponse.

4. Conclusion

To conclude, we have demonstrated how encapsulated graphene can be coupled to plasmonic nanostructures via 1D edge contacts in order to enhance its optical response, while still maintaining the high-room temperature mobilities, robustness, and chemical stability associated with hBN-encapsulated graphene devices. We report very large responsivities across the visible regime, in the order of hundreds of A/W, although we do see the device rapidly saturating for incident optical powers of just a few μW. We report NEP of $\approx 100\ \mathrm{pW}/\sqrt{\mathrm{Hz}}$ for low incident power.

We also observe an unexplained photogating effect in our devices. While we are not strictly able to confirm it, we suspect that it may be related to defect states in the encapsulated hBN flakes. These defects are likely created during the fabrication process, which involves exposing the hBN to a high-energy electron beam and an RIE process involving O_2 and CHF_3 plasmas.[34] Such defects could emulate quantum dots, which in the past have been observed to cause a photogating effect in graphene.[1,37]

5. Experimental Section

Device Fabrication: hBN multilayers and graphene monolayers (NGS Naturgraphit) were mechanically exfoliated onto silicon substrates with 285 nm thermal oxide. From here they were picked up and stacked into hBN/graphene/hBN heterostructures at 100 °C using a home-built 2D material transfer system with a heating stage[17] using PC/PDMS polymer stamps.[28] After heterostructure assembly, the stacks were dropped off on a clean silicon substrate (highly p-doped) with a 285 nm thermal oxide on top by melting the PC sacrificial layer at 200°. The samples were then cleaned by soaking them in $CHCl_3$ to remove PC residues. Next, the samples are spin coated with ≈450 nm of PMMA, and electron beam lithography (Elionix) was used to pattern the metasurface structures and the contact pads in the PMMA resist. The resist pattern was then etched into the hBN/graphene/hBN layers using RIE with a mix of O_2 and CHF_3.[27] The samples were then moved to an electron beam evaporator vacuum chamber where they were left overnight until the chamber pressure reached $\approx 10^{-8}$ bar. Then, 10 nm of Cr followed by 120 nm of Au was evaporated, followed by lift-off in warm acetone.

FDTD Simulations: Periodic arrays of gold nanodisks embedded into hBN/graphene/hBN stacks were simulated using the commercial Lumerical FDTD software package (Ansys). Periodic boundary conditions were used for the *x*- and *y*-axes, and the top and bottom of the *z*-axis were terminated with perfectly matched layers. Light was injected as a plane-wave source from above the nanodisk, propagating along the negative *z*-direction. A reflection source monitor was positioned behind the source, and an absorption monitor was placed to encapsulate the whole of the graphene/gold volumes. The nanodisks had a diameter of 400 nm, with a unitcell period of 500 nm. The substrate consisted of 285 nm SiO_2 followed by an infinite layer of Si. Standard materials from the Lumerical library were used.

Responsivity and Electrical Measurements: Device responsivity was measured using a home-built reflection microscope and electrical probe station. The sample was excited using a SuperK Extreme supercontinuum laser (NKT Photonics) monochromated to a spectral width of ≈4 nm around a central wavelength using a LLTF SWIR-HP8 filter (Fianium). The laser was coupled through the reflection microscope, and the excitation power was controlled using two linear polarization filters, with the last filter remaining in a fixed position to maintain the laser polarization hitting the sample. Electrical contacts to the source and drain were made using tungsten probes and 3D stage micromanipulators, while the back gate to the silicon was achieved by scratching the back of the Si chip and adhering to the holder via conductive silver paint, and source–drain and bias voltage were applied using a two-channel B2902A source measure unit (Keysight), with the same unit monitoring the source–drain current during the gate sweep.

Optical Reflection Measurements: Optical reflection spectra of the metasurface devices were measured by illuminating the samples with a white light source (tungsten–halogen lamp) through a microscope objective (Nikon, 50×, NA 0.45), and the reflected light was collected with the same objective. The light was then spatially filtered with an aperture at the image plane of the objective to collect light only from the device area to an Ocean Optics Flame spectrometer. The recorded reflection spectra were normalized to a gold mirror.

Supporting Information

Supporting Information is available from the Wiley Online Library or from the author.

Acknowledgements

C.F. was supported by the Carlsberg Foundation as an Internationalisation Fellow during this work.

Conflict of Interest

The authors declare no conflict of interest.

Author Contributions

The project idea was conceived of by C.F. and U.L. Heterostructure assembly was done by C.F., S.R.K.C.I., and T.R.D. hBN was synthesized by K.W. and T.T. E-beam lithography and electrode fabrication were done by N.M., Z.H., and C.F. Scanning electron microscopy images were recorded by Z.H. Optical and electrical device characterization was done by C.F. Optical simulations were done by C.F. The manuscript was written by C.F. with input from all authors. H.S. and U.L. supervised the work.

Data Availability Statement

The data that support the findings of this study are available from the corresponding author upon reasonable request.

Keywords

grapehene, hBN defects, hot carriers, photodetections, plasmonics

Received: December 15, 2023
Revised: January 12, 2024
Published online: February 2, 2024

---

[1] F. H. L. Koppens, T. Mueller, P. Avouris, A. C. Ferrari, M. Serena Vitiello, M. Polini, *Nat. Nanotechnol.* **2014**, *9*, 780.
[2] A. Elbanna, H. Jiang, Q. Fu, J. F. Zhu, Y. Liu, M. Zhao, D. Liu, S. Lai, X. W. Chua, J. Pan, Z. X. Shen, *ACS Nano* **2023**, *17*, 4134.
[3] C. Liu, J. Zheng, Y. Chen, T. Fryett, A. Majumdar, *Opt. Mater. Express* **2019**, *9*, 384.
[4] T. Mueller, F. Xia, P. Avouris, *Nat. Photonics* **2010**, *4*, 297.
[5] S. Cakmakyapan, P. K. Lu, A. Navabi, M. Jarrahi, *Light: Sci. Appl.* **2018**, *7*, 20.
[6] Y. Ding, Z. Cheng, X. Zhu, K. Yvind, J. Dong, M. Galili, H. Hu, N. Asger Mortensen, S. Xiao, L. K. Oxenløwe, *Nanophotonics* **2020**, *9*, 317.
[7] S. Narayan, S. Yadav, P.-L. Chen, C. H. Liu, T.-J. Yen, *Adv. Mater. Interfaces* **2023**, *10*, 2202403.
[8] J. Yan, M. H. Kim, J. A. Elle, A. B. Sushkov, G. S. Jenkins, H. M. Milchberg, M. S. Fuhrer, H. D. Drew, *Nat. Nanotechnol.* **2012**, *7*, 472.
[9] D. K. Efetov, R. J. Shiue, Y. Gao, B. Skinner, E. D. Walsh, H. Choi, J. Zheng, C. Tan, G. Grosso, C. Peng, J. Hone, *Nat. Nanotechnol.* **2018**, *13*, 797.
[10] A. Blaikie, D. Miller, B. J. Alemán, *Nat. Commun.* **2019**, *10*, 4726.
[11] J. Gosciniak, J. B. Khurgin, *ACS Omega* **2020**, *5*, 14711.
[12] S. Yuan, R. Yu, C. Ma, B. Deng, Q. Guo, X. Chen, C. Li, C. Chen, K. Watanabe, T. Taniguchi, F. J. Garcia de Abajo, *ACS Photonics* **2020**, *7*, 1206.
[13] V. Mišeikis, S. Marconi, M. A. Giambra, A. Montanaro, L. Martini, F. Fabbri, S. Pezzini, G. Piccinini, S. Forti, B. Terrés, I. Goykhman, *ACS Nano* **2020**, *14*, 11190.
[14] S. Schuler, J. E. Muench, A. Ruocco, O. Balci, D. V. Thourhout, V. Sorianello, M. Romagnoli, K. Watanabe, T. Taniguchi, I. Goykhman, A. C. Ferrari, *Nat. Commun.* **2021**, *12*, 3733.
[15] D. A. Bandurin, D. Svintsov, I. Gayduchenko, S. G. Xu, A. Principi, M. Moskotin, I. Tretyakov, D. Yagodkin, S. Zhukov, T. Taniguchi, K. Watanabe, *Nat. Commun.* **2018**, *9*, 5359.
[16] I. Gayduchenko, S. G. Xu, G. Alymov, M. Moskotin, I. Tretyakov, T. Taniguchi, K. Watanabe, G. Goltsman, A. K. Geim, G. Fedorov, D. Svintsov, *Nat. Commun.* **2021**, *12*, 543.
[17] C. Frydendahl, S. R. K. Chaitanya Indukuri, M. Grajower, N. Mazurski, J. Shappir, U. Levy, *ACS Photonics* **2021**, *8*, 2659.
[18] I. Goykhman, U. Sassi, B. Desiatov, N. Mazurski, S. Milana, D. De Fazio, A. Eiden, J. B. Khurgin, J. Shappir, U. Levy, A. C. Ferrari, *Nano Lett.* **2016**, *16*, 3005.
[19] R. Gherabli, S. R. K. C. Indukuri, R. Zektzer, C. Frydendahl, U. Levy, *Light: Sci. Appl.* **2023**, *12*, 60.
[20] R. R. Nair, P. Blake, A. N. Grigorenko, K. S. Novoselov, T. J. Booth, T. Stauber, N. M. R. Peres, A. K. Geim, *Science* **2008**, *320*, 1308.
[21] S. Thongrattanasiri, F. H. L. Koppens, F. J. G. De Abajo, *Phys. Rev. Lett.* **2012**, *108*, 047401.
[22] S. Xiao, X. Zhu, B.-H. Li, N. Asger Mortensen, *Front. Phys.* **2016**, *11*, 117801.
[23] Z. Fang, Z. Liu, Y. Wang, P. M. Ajayan, P. Nordlander, N. J. Halas, *Nano Lett.* **2012**, *12*, 3808.
[24] J. E. Muench, A. Ruocco, M. A. Giambra, V. Miseikis, D. Zhang, J. Wang, H. F. Y. Watson, G. C. Park, S. Akhavan, V. Sorianello, M. Midrio, *Nano Lett.* **2019**, *19*, 7632.
[25] P. Ma, Y. Salamin, B. Baeuerle, A. Josten, W. Heni, A. Emboras, J. Leuthold, *ACS Photonics* **2018**, *6*, 154.
[26] Z. Ma, K. Kikunaga, H. Wang, S. Sun, R. Amin, R. Maiti, M. H. Tahersima, H. Dalir, M. Miscuglio, V. J. Sorger, *ACS Photonics* **2020**, *7*, 932.
[27] L. Wang, I. Meric, P. Y. Huang, Q. Gao, Y. Gao, H. Tran, T. Taniguchi, K. Watanabe, L. M. Campos, D. A. Muller, J. Guo, P. Kim, J. Hone, K. L. Shepard, C. R. Dean, *Science* **2013**, *342*, 614.
[28] F. Pizzocchero, L. Gammelgaard, B. S. Jessen, J. M. Caridad, L. Wang, J. Hone, P. Bøggild, T. J. Booth, *Nat. Commun.* **2016**, *7*, 11894.
[29] Y. Cao, V. Fatemi, S. Fang, K. Watanabe, T. Taniguchi, E. Kaxiras, P. Jarillo-Herrero, *Nature* **2018**, *556*, 43.
[30] Y. Matsuda, W.-Q. Deng, W. A. Goddard III, *J. Phys. Chem. C* **2010**, *114*, 17845.
[31] D. S Schulman, A. J Arnold, S. Das, *Chem. Soc. Rev.* **2018**, *47*, 3037.
[32] Z. Fang, Y. Wang, Z. Liu, A. Schlather, P. M. Ajayan, F. H. L. Koppens, P. Nordlander, N. J. Halas, *ACS Nano* **2012**, *6*, 10222.
[33] G. Prakash, R. K. Srivastava, S. N. Gupta, A. K. Sood, *J. Chem. Phys.* **2019**, *151*, 234712.
[34] M. Fischer, J. M. Caridad, A. Sajid, S. Ghaderzadeh, M. Ghorbani-Asl, L. Gammelgaard, P. Bøggild, K. S. Thygesen, A. V. Krasheninnikov, S. Xiao, M. Wubs, *Sci. Adv.* **2021**, *7*, abe7138.
[35] T. R. Devidas, I. Keren, H. Steinberg, *Nano Lett.* **2021**, *21*, 6931.
[36] K. S. Novoselov, A. K. Geim, S. V. Morozov, D. Jiang, Y. Zhang, S. V. Dubonos, I. V. Grigorieva, A. A. Firsov, *Science* **2004**, *306*, 666.
[37] G. Konstantatos, M. Badioli, L. Gaudreau, J. Osmond, M. Bernechea, F. De Arquer, F. Gatti, F. H. L. Koppens, *Nat. Nanotechnol.* **2012**, *7*, 363.
[38] P. Bøggild, D. M. A. Mackenzie, P. R. Whelan, D. H. Petersen, J. D. Buron, A. Zurutuza, J. Gallop, L. Hao, P. U. Jepsen, *2D Mater.* **2017**, *4*, 042003.
[39] E. Glushkov, M. Macha, E. Räth, V. Navikas, N. Ronceray, C. Y. Cheon, A. Ahmed, A. Avsar, K. Watanabe, T. Taniguchi, I. Shorubalko, A. Kis, G. Fantner, A. Radenovic, *ACS Nano* **2022**, *16*, 3695.
[40] J. Horder, S. J. U. White, A. Gale, C. Li, K. Watanabe, T. Taniguchi, M. Kianinia, I. Aharonovich, M. Toth, *Phys. Rev. Appl.* **2022**, *18*, 064021.
[41] S. Gao, H.-Y. Chen, M. Bernardi, *npj Comput. Mater.* **2021**, *7*, 85.
[42] W. Liu, N.-J. Guo, S. Yu, Y. Meng, Z. Li, Y.-Z. Yang, Z.-A. Wang, X.-D. Zeng, L.-K. Xie, J.-F. Wang, *Mater. Quantum Technol.* **2022**, *2*, 032002.
[43] P. Auburger, A. Gali, *Phys. Rev. B* **2021**, *104*, 075410.
[44] H. J. Kim, K. J. Lee, J. Park, G. H. Shin, H. Park, K. Yu, S.-Y. Choi, *ACS Appl. Mater. Interfaces* **2020**, *12*, 38563.